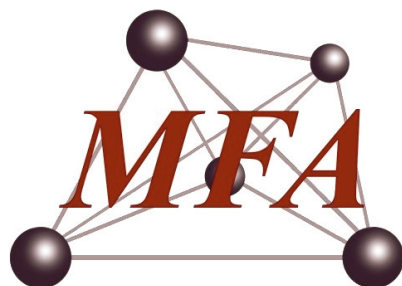


Hungarian Academy of Sciences  
Research Centre for Natural Sciences

# Yearbook

2014



**Institute of Technical Physics  
and Materials Science**

<http://www.mfa.kfki.hu/>

## ***Microtechnology Department***

**Head: Gábor BATTISTIG, Ph.D., senior research fellow**

### **Research Staff**

- Zsófia BAJI, Ph.D.
- István BÁRSONY, Corr. Member of HAS
- Gábor BATTISTIG, Ph.D.
- László DÓZSA, Ph.D.
- Csaba DÜCSŐ, Ph.D.
- Zoltán FEKETE, Ph.D. (on leave)
- Péter FÖLDESZ, Ph.D.
- Péter FÜRJES, Ph.D.
- Zoltán HAJNAL, Ph.D.
- Nguyen Quoc KHÁNH, Ph.D.
- Zoltán LÁBADI, Ph.D.
- István LUKÁCS, Ph.D.
- György MOLNÁR, Ph.D.
- Ákos NEMCSICS, D.Sc. (part time)
- Andrea Edit PAP, Ph.D. (part time)
- Anita PONGRÁCZ, Ph.D. (on leave)
- Vilmos RAKOVICS, Ph.D.
- Attila Lajos TÓTH, Ph.D.
- János VOLK, Ph.D.
- Zsolt ZOLNAI, Ph.D.

### **Ph.D. students**

- Zsófia BÉRCZES
- Zoltán SZABÓ)
- Ferenc BÍRÓ
- Máté TAKÁCS
- Róbert ERDÉLYI
- Gergely MÁRTON
- Tamás KÁRPÁTI
- Eszter HOLCZER
- Eszter TÓTH

### **Technical Staff**

- János FERENCZ (engineer)
- Levente ILLÉS (engineer)
- Csaba LÁZÁR (engineer)
- István RÉTI (engineer)
- Róbert HODOVÁN (engineer)
- András LŐRINCZ (engineer)
- Erika TUNYOGI (engineer)
- Katalin VERESNÉ VÖRÖS (engineer)
- György ALTMANN (technician)
- Gabriella BÍRÓ (technician)
- Sándor CSARNAI (technician)
- Tibor CSARNAI (technician)
- Magda ERŐS (technician)
- Károlyné PAJER (technician)
- Csilla ARIAS-SOTONÉ FARAGÓ (technician)
- Attila NAGY (technician)
- Magda VARGA (technician)

## **The task of the Microtechnology Department is:**

### ***Fundamental research on***

- sensing principles;
- novel materials and nanostructures;
- novel 3D fabrication techniques;
- ion-solid interaction for supporting MEMS development.

### ***Research and development of physical, chemical/biochemical sensors and integrated systems:***

- R&D on micropellistor-type gas sensors, 3D force sensors, thermal sensors, gas flow sensors, using CMOS compatible and related techniques - **MEMS**.
- Development of novel microfluidic systems, their application in new fields of biochemistry - **BioMEMS**.
- Development of Si- and polymer based sensors for biomedical applications with special focus on neuroscience - **NeuroMEMS**.
- Synthesis and characterization of quasi-one-dimensional semiconducting nanostructures, semiconductor nanodevices, their integration into functional sensors, optoelectronic and photovoltaic devices - **NEMS**.

### ***Modelling, structural and device characterization methods:***

- Electrical characterization;
- Thermo-mechanical characterization;
- Scanning Microprobes;
- Ion beam analysis methods;
- SEM, TEM, EDX;
- Spectroscopic Ellipsometry.

The Department runs two 300 m<sup>2</sup> + 160 m<sup>2</sup> clean labs (Class 100-10000) comprising *a complete Si-CMOS processing line and a mask shop*, unique facility in Hungary. The technology allows to manufacture layers, patterned structures and devices with 1 μm line resolution on 3” and 4” Si and glass wafers.

**Competencies** (available also for our industrial and academic partners and customers):

- High temperature annealing, diffusion and oxidation;
- Ion implantation;
- Rapid Thermal Treatment;
- Low Pressure Chemical Vapor Deposition of poly-Si, SiO<sub>2</sub> and Si<sub>3</sub>N<sub>4</sub> layers;
- Low Temperature Chemical Vapor Deposition;
- Atomic Layer Deposition;
- Physical Vapor Deposition – Electron beam evaporation, DC and RF Sputtering;

- Reactive Ion Etching, Deep Reactive Ion Etching;
- Photolithography with back-side alignment and Nanoimprinting;
- E-beam lithography;
- Nanopatterning, deposition and etching by Focused Ion-Beam;
- Wafer-bonding;
- Wet chemical treatments;
- Electro-chemical porous Si formation;
- Molecular Beam Epitaxy of III-V compound semiconductors;
- Mask design, laser pattern generator;
- Polymer (PDMS, SU8, Polyimide) structuring by photolithography and micro-molding techniques,
- Chip dicing, packaging especially for sensor applications;
- Materials and structural analysis & characterization:, SEM, FIB, EDX, Atomic Force Microscopy, Electrochemical Impedance Spectroscopy, Stylus Profiler;
- Electrical and functional characterization.



For detailed information please visit our website: [www.mems.hu](http://www.mems.hu)

or contact us by e-mail: [dragon@mfa.kfki.hu](mailto:dragon@mfa.kfki.hu)

# Transducer development for continuous on-site monitoring of hydrocarbon content dissolved in underground and waste-water

(KMR\_12-1-2012-0107)

V. Rakovics, Cs. Dücső, and G. Battistig

Project partner: WESZTA-T Industrial and commercial Ltd.

## Goal of the development:

Hydrocarbon contamination heavily deteriorates the quality of underground, natural and waste water, therefore its control is essential to avoid environmental accidents. The project aims at the development of transducers capable to detect petrol and diesel oil contamination of 0 – 100 ppm range in monitoring wells around storage tanks, filling stations as well as in industrial waste water disposals.

## Achievements:

UV photoluminescence measurement was selected as operation principle of the device. The method is based on the luminescence of the aromatic components (benzene, its relatives and poly-aromatics, PAH) present in both fuels. Note, that while petrol contains up to 30v% PAHs and highly soluble benzene up 1%, diesel oil is characterized by PAHs of 10-11v%. Therefore any difference in their absorption and luminescence properties may open the way towards selective measurements.

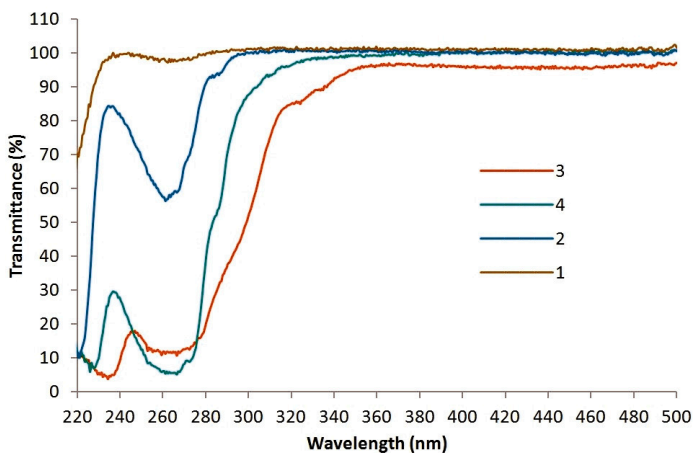


**Figure 1** Transmittance spectra of petrol and diesel oil dissolved in DI water and methanol. 100 ppm diesel oil in water (1), 200 ppm petrol in water (2), 500 ppm diesel oil in methanol (3), 500 ppm petrol in methanol (4).

The sensor development started with detailed experimental measurements to determine the optimum excitation and detection frequencies for both petrol and diesel oil as dissolved in water. UV excitation proved to be the best effective in the 250-280 nm range with maximum of 265 nm (Fig. 1).

For detection of diesel oil the 310–340 nm range with optimum wavelength of 320 nm is ideal, while petrol has characteristic luminescence peaks in the 290-310 nm and in the 320–340 nm ranges (Fig. 2). Although the luminescence peaks overlap, the difference shown in Fig. 2 offers the possibility to fabricate a sensor optimized for any of these materials and capable to distinguish between them.

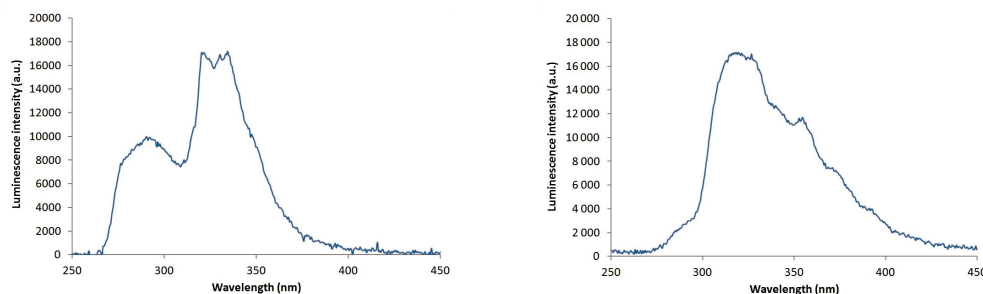


**Figure 2** Luminescence spectra of diesel oil (a) and gasoline (b) taken by high integration time and excitation at 270 nm. Concentration of diesel oil and gasoline in DI water were 100 and 500 ppm, respectively.

Several geometric arrangements, all based on perpendicular excitation and detection light paths, were modelled with consideration the size limitations of the complete device. Keeping always in mind the targeted low production cost and technical specifications (sensitivity, stability, reproducibility and life-time of the device) a careful selection of critical components was made backed by detailed test measurements in our laboratory. UV LED was selected on basis of the emission spectra, light intensity and shape of cone as well as life time and long term stability of alternative devices. Similarly, several detectors were characterized by their spectral sensitivity, total current, stability and life time. The complex investigation led to the final selection of all the optical elements the sensor head was formed from.

The sensor (Fig. 3) consists of a UV LED with directional light path and two identical UV detectors arranged perpendicularly to the excitation light. A common glass window in front of the detectors cuts off the short wavelength of the excitation, therefore eliminates direct interference. An additional glass filter in front of one of the detectors cuts off the wavelength below 320 nm of the luminescent spectrum. Thereby the signal ratio of the two detectors enables us to identify the type of contamination, i.e. to distinguish petrol or diesel oil. Our measurements also revealed that there is no interference with detergents or algae with this construction.

The drive and read-out electronics, the communication port and the proper encapsulation was developed by the cooperating partner WESZTA-T Ltd.

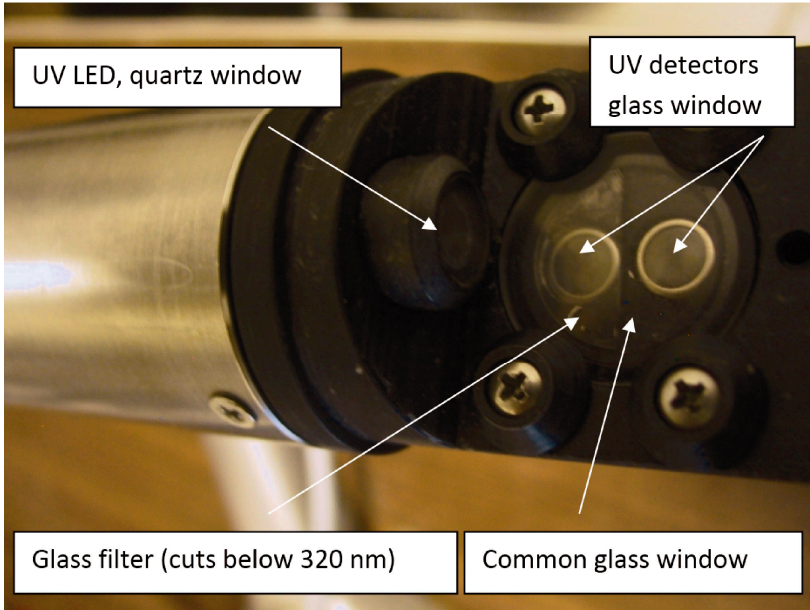


**Figure 3** Optical arrangement of the sensor head. Cover for protection against mechanical damage and external light excitation is removed.

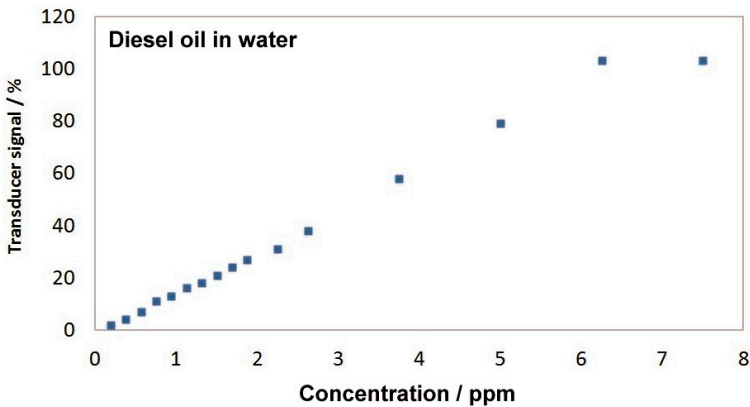


**Figure 4** Transducer signal. Sensor is calibrated for detection of diesel oil dissolved in water. Solubility limit at 8ppm.

With proper calibration the sensor can be set for detecting petrol or diesel oil. Fig. 4 represents the sensor signal as calibrated for measuring gasoline dissolved in water. Three of these transducers were installed by WESZTA-T Ltd. for final on-site testing at a large oil storage plant.

## **MEMS**

*Activity leader:* Cs. Dücső

*Group members:* Zs. Baji, I. Bársony, G. Battistig, L. Dózsa, P. Földesy, P. Fürjes, Z. Hajnal, Z. Lábadi, Gy. Molnár, A. E. Pap, V. Rakovics, A. L. Tóth, E. Tunyogi, Zs. Zolnai, F. Biró, T. Kárpáti, and M. Takács

### **Projects are supported by:**

- OTKA K109674 - Graphen based terahertz modulators (2013-2017)
- KMR\_12-1-2012-0107 - Sensor for continuous monitoring of carbonhydrides dissolved in underground water (2012-2015)
- KMR\_12-1-2012-0226 – Development of components of the new generation of neutron detecting instruments (2012-2015)
- KMR\_12-1-2012-0031 - Development of an embedded information system for the optimisation of energy-positive public lighting (2012-2014)
- TÉT\_10-1-2011-0305 – Development of tungsten and molybdenum oxide thin films for use in gas sensors and electro chromic devices (2012-2014)

## **Development of Embedded Information Technology System to optimize Energy-positive Public Lighting**

The main goal of the development is construction of a public lighting system of minimum energy consumption and positive energy balance by development and integration of individual components, e.g. LED street lamps, renewable energy generation and storage system as well as control SW for intelligent operation. Our group developed a weather station for recording data base to be used in short time prediction of weather conditions and energy management planning. Additionally, we have to characterize commercial PV modules in terms of their long-term energy generation and readiness throughout the day. Module types and installation methods are investigated in detail.

The demonstration system was installed alongside roads and pathways at the KFKI campus by retrofitting conventional lighting armatures with novel LED luminaries produced by GE. Each street lamp has its own motion sensor to detect and distinguish automotive or pedestrian presence. Moreover, the lighting system is capable to adjust the pre-programmed lighting scenario according to the actual situation by using the ability of luminaries to communicate via WiFi.

The system is completely automated and controlled via internet from a central computer. The required energy is centrally generated and stored by solar panels and

batteries, respectively. The grid connected power system covers the total energy needed, but is also able to control energy flow in both directions. The driving SW calculates the optimum energy flow by considering the predicted energy generation and also the actual price of electricity (Fig 1).

In order to provide appropriate data both for PV module characterization and short term weather forecast a complex weather sensor station was constructed. Two irradiation sensors measure the global and diffuse irradiation. Additionally, air pressure, humidity, temperature and wind speed are also registered (Fig 2). A twilight sensor provides data for on-off switching the street lighting system. The sensor chip of the air pressure sensor and the system were developed and constructed by the MEMS lab of MFA.

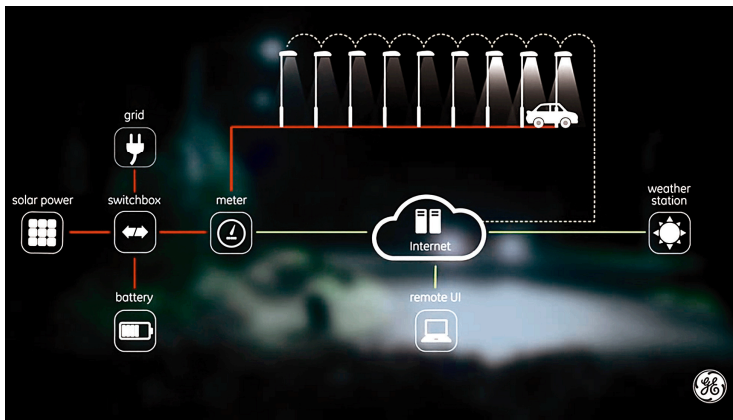


**Figure 1** Schematics of the smart street lighting system. (with permission of GE Lighting).



**Figure 2** Integrated weather station on the roof of MEMS lab. building.

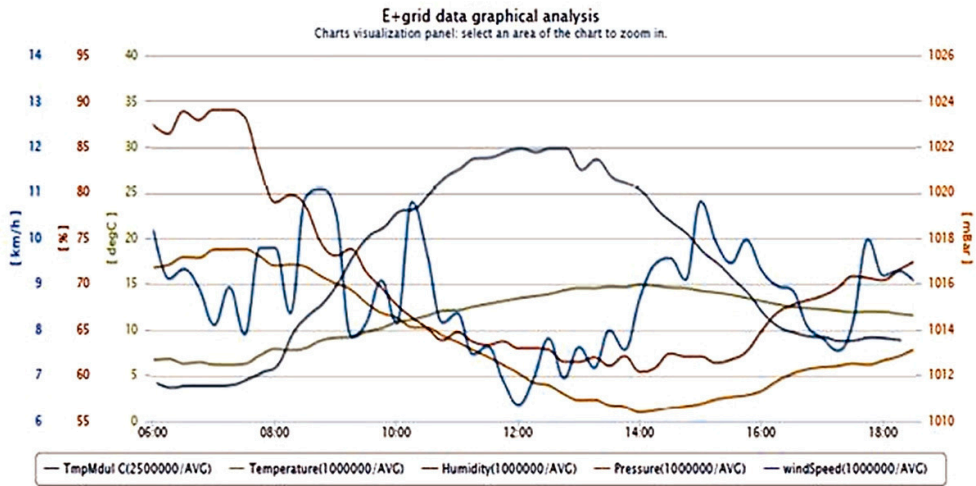


**Figure 3** PV module, air temperature, humidity, pressure and wind speed recorded on November 4, 2014.

### Long-term characterization of PV modules

A test station was constructed for investigation of long-term energy production of commercial PV modules and the effect of installation method. Beside crystalline Si modules thin film amorphous Si, micromorph-Si, CdTe and CIGS modules were installed at 3 positions: fixed  $12^\circ$  and  $42^\circ$  tilted,  $30^\circ$  tilted on a one axis east-west solar tracker (Fig. 4). Drawing consequences require a year-long measurement at least, here we only demonstrate the effects of module positions (Fig. 6).



**Figure 4** PV modules installed by different tilting. Fixed  $12^\circ$  and  $42^\circ$  (right) and on a  $30^\circ$  single axis tracker (left). Modules c-Si, a-Si, CIS, CdTe and micromorph-Si on  $42^\circ$  from left to right.

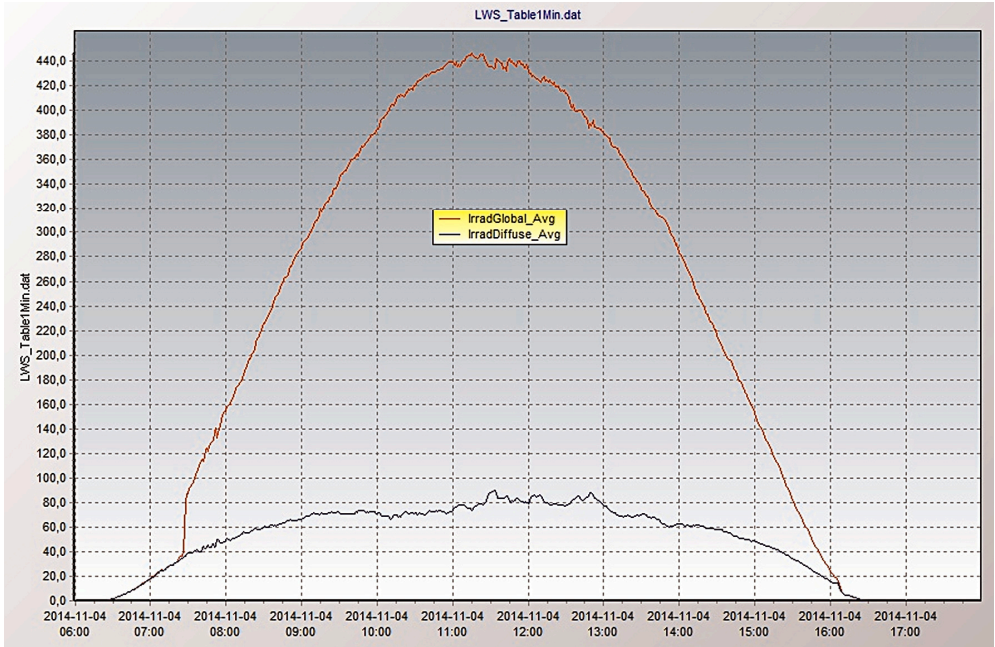


**Figure 5** Global (red) and diffuse (blue) irradiation on the clear, sunny day of November 4, 2014.

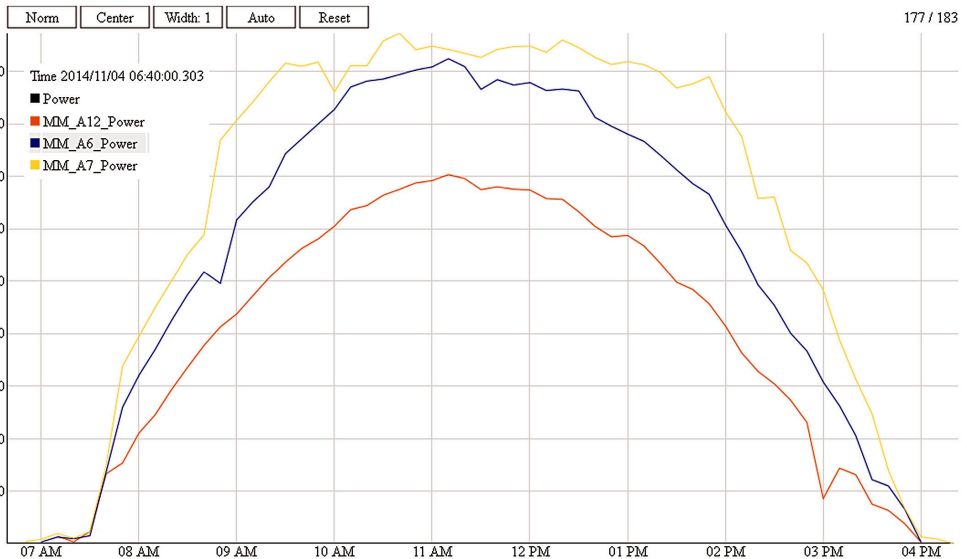


**Figure 6** Power produced by three identical micromorph-Si modules on November 4, 2014. 12° tilted (red), 42° tilted (blue) and 30° tilted on the solar tracker (yellow) clearly demonstrates the difference.

## Quantitative compositional analysis of BeMgZnO alloys using the combination of nondestructive ion beam techniques

ZnO and related BeMgZnO alloys received recently considerable attention due to their promising optical and electrical properties for application in optoelectronic devices, e.g. light emitting diodes and solar-blind UV detectors. Although theoretical studies on bandgap variation and equilibrium lattice parameters for the BeMgZnO system were performed, no considerable attention was paid to the systematic quantitative comparison of measured and calculated properties vs. Be and Mg concentrations. Instead of previously applied analytical techniques like SIMS or XPS, which require sample standards, lead to sputtering and sample damage effects, and suffer from limitations in the detection of the light element Be, we apply ion beam analysis as a nondestructive characterization tool.

In this work the atomic composition with less than 1-2 at% uncertainty was measured in plasma assisted molecular beam epitaxy grown BeZnO and BeMgZnO alloys using Rutherford Backscattering Spectrometry with  $\text{He}^+$  ions (He-RBS) and Non-Rutherford Elastic Backscattering Spectrometry with protons (p-EBS), see Fig. 1 and Fig. 2. In p-EBS an enhancement factor of 60 in the cross-section of Be was achieved, allowing quantitative depth profiling and compositional analysis based on a multiple spectrum fit evaluation procedure.

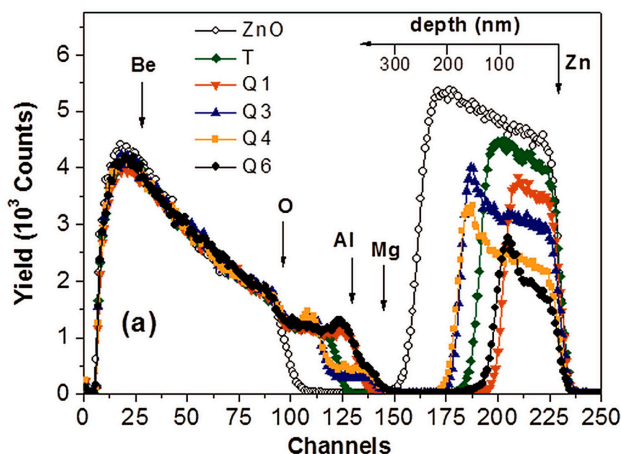


**Figure 1** 1 MeV  $\text{He}^+$ -RBS spectra of ZnO, BeZnO (T), and BeMgZnO (Q1, Q3, Q4, Q6) layers, grown on sapphire. Surface edges for Be, O, Mg, and Zn, and the spectrum edge for buried Al (in sapphire) are indicated. The depth scale for Zn is also shown.

Eight different samples were analyzed: one reference ZnO, one BeZnO (T), and six BeMgZnO (Q1-Q6) layers. The layer compositions were found to be  $\text{Be}_{0.08}\text{Zn}_{0.92}\text{O}$  (T),  $\text{Be}_{0.11}\text{Mg}_{0.14}\text{Zn}_{0.75}\text{O}$  (Q1),  $\text{Be}_{0.08}\text{Mg}_{0.30}\text{Zn}_{0.62}\text{O}$  (Q2),  $\text{Be}_{0.07}\text{Mg}_{0.33}\text{Zn}_{0.60}\text{O}$  (Q3),  $\text{Be}_{0.07}\text{Mg}_{0.46}\text{Zn}_{0.47}\text{O}$  (Q4),  $\text{Be}_{0.19}\text{Mg}_{0.42}\text{Zn}_{0.39}\text{O}$  (Q5), and  $\text{Be}_{0.12}\text{Mg}_{0.52}\text{Zn}_{0.36}\text{O}$  (Q6), respectively. Based on the measured atomic compositions, hybrid density functional (HDF) bandgap calculations were performed and compared to experimental optical bandgaps. The theoretical vs. experimental values show linear correlation in the entire bandgap range studied from 3.26 eV to 4.62 eV, according to Fig. 3. In summary, the

analytical method employed should help to facilitate bandgap engineering for potential applications, such as solar blind UV photodetectors and heterostructures for UV emitters and inter-sub-band devices.

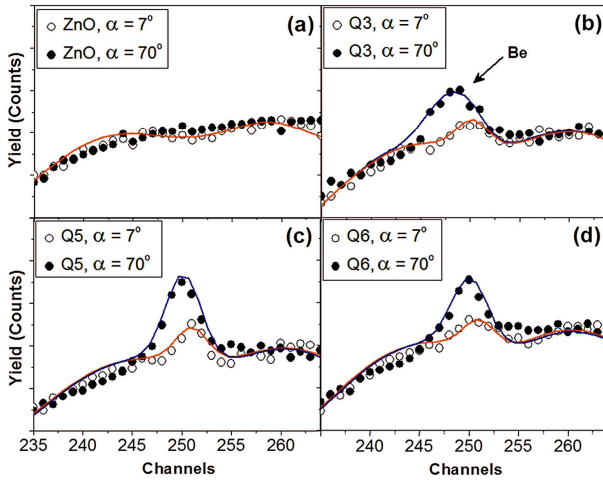


**Figure 2** Beryllium peak regions of 2.53 MeV p-EBS spectra for (a) ZnO, and BeMgZnO layers (b) Q3, (c) Q5, and (d) Q6, respectively, measured at sample tilt angles of  $\alpha = 7^\circ$  and  $\alpha = 70^\circ$ . The symbols represent measured data. Simulated spectra by red and blue lines are also shown.

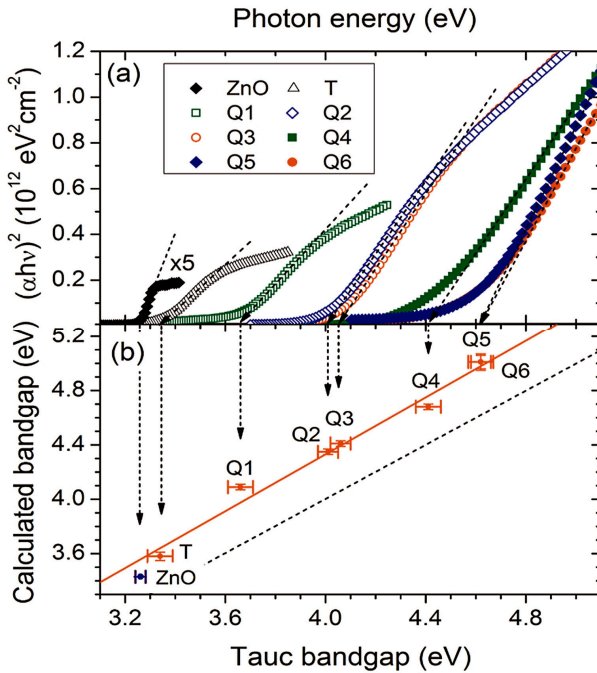


**Figure 3** (a) Tauc plots of absorption edges deduced from optical transmittance measurements and (b) comparison of the experimental optical and calculated bandgaps for the studied ZnO, BeZnO (T), and BeMgZnO (Q1-Q6) samples. HDF calculations are based on Mg and Be concentrations extracted from He<sup>+</sup>-RBS and p-EBS analysis. The solid red line is the linear fit to red dots. The dashed line shows the one-to-one function.

### **3D force sensors for minimal invasive surgery applications**

Minimal invasive surgery gives a chance for many patients (over 4 million a year) for faster recovery, shorter hospitalization, less risk of complications and less traumas to healthy tissues during surgery. For a large group of patients it is the only way for surgery because of the substantial risk of following the classical way. When mechanical laparoscopic tools are used, increasing the distance of the surgeon's hand from the patient's body reduces the sense of touch, which, however, is pivotal for the surgeon to assess the condition of the tissues and also for precise control of the tools. Currently surgical robots are not equipped with effective technical means of measuring forces during treatment, so during telemanipulation the surgeon is deprived of much important actual information from operation field.

The INCITE project is intended to reveal and explore the advantages of the integration and application of various sensing capabilities in Minimal Invasive Surgery (catheter or surgery robot) systems. These subsystems are applicable to extend the functionality of the medical systems by improving feedback for the operators and surgeons during the intervention. The future aim is to improve the functional characteristics, safety and standards of medical devices (catheters, robotic tools) applicable to minimal invasive cardiac intervention and surgery.

Accordingly, our goals were the design, realization and integration of 3D contact force sensors / sensor arrays into surgical robotics demonstrators and the feasibility study of the application of MEMS based contact force measurements in cardiac ablation catheters. The partners MFA and FRK (Fundacja Rozwoju Kardiochirurgii) decided to focus on the following three implementations of the targeted MEMS force sensors as presented in Fig. 1:

- as touch sensor in the front part of the tool giving the surgeon the opportunity to palpation, evaluation of touch operations in the area of tissue (typically between force values of 0 and 1 N),
- as tool holder sensor giving surgeon the opportunity to assess the range of force of tissue clamp (reducing the risk of destruction), measuring the strength of the manipulation (e.g. measuring the force when engaging in a surgical knot, typical force range up to 10 N) and forces capture surgical needles or other technical element used during operation (up to 100 N),
- as a sensor of interface robot control system, operating in force control mode, giving the surgeon a chance to control the position of the endoscopic vision system using a robot Robin Heart Vision during classical operations using laparoscopic tools (mini joystick mounted in the handle tools or mini remote control), or for positioning the arm root (mini-joystick mounted on the robot arm).

#### **Tactile sensing systems**

Tactile sensors are commonly used in industrial, medical or virtual-reality applications, but the majority of commercial tactile systems are able to detect pressure

maps only. The MEMS 3D force sensing device proposed within the INCITE processes all three axial (normal and shear) components of the tactile information at every sensory element (taxel – tactile pixel). Furthermore, in contrast to conventional optical devices, this force sensor allows integration of multiple sensors, actuators and electronics (ASIC) at the catheter tip. Deplorability of elements of a novel tactile sensing array will be investigated within INCITE with the final goal to mimic the operation of real biological sensing-processing system with artificial tactile sensors that could be integrated into Minimally Invasive Surgical (MIS) Robotic systems.

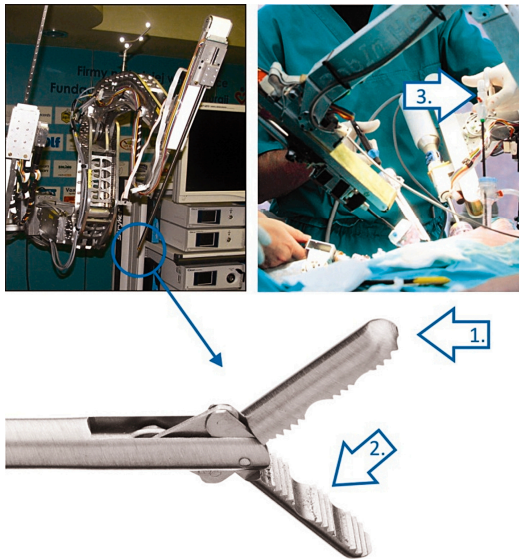


*Figure 1* The representation of the proposed applications of the vectorial force sensor in Minimal Invasive Surgery robot systems.

Based on the literature data and our previous experience the piezoresistive read-out principle was selected to detect the vectorial force and the mechanical deformations. SOI (silicon-on-insulator) basic substrate was selected and adopted for MEMS structure fabrication with combination with Deep Reactive Ion Etching 3D micromachining technology to achieve precise geometric control of the membrane considering the strong geometry dependence of the device sensitivity and working range. This DRIE technique enables to decrease the final chip size due to the high aspect ratio sidewall structuring. Preliminary test devices for the robot control application were fabricated and delivered to our partner (FRK) for functional characterization.

#### FEM modelling of the device

For determination the precise geometric parameters (membrane thickness, lateral geometry) and the sensitivity of the embedded piezoresistors Finite Element Model was developed and studied in details. Note, the encapsulation (electronic packaging, biocompatible coverage) of the sensor chips can remarkably modify the final sensitivity of the device. Therefore we have started a detailed experimental work to

reveal the effect of the biocompatible elastic coating. The complexity of the task is manifested in the effect on the mechanical properties (force transfer, hysteresis, introduced thermal stress), while the coating must withstand the environment of the sterilization in several times.

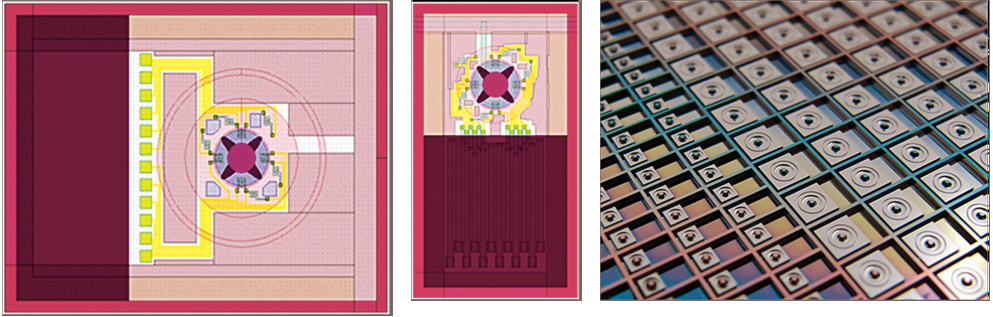


Figure 2 Layout of the developed force sensors and the fabricated elements.

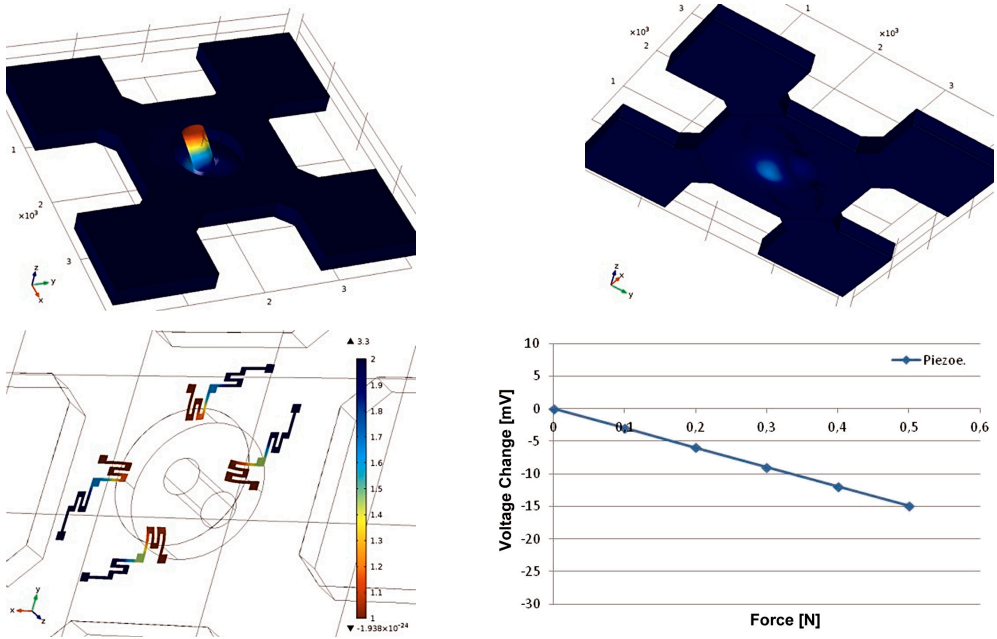


Figure 3 Mechanical and multi-physical modelling of the force sensor structure can forecast the functional parameters of the device. Deformation and stress distribution of the embedded piezoresistors is applicable to deduce the estimated signal vs. applied force function of the force sensor of given geometries.

## ***BioMEMS & Microfluidics***

*Activity leader:* P. Fürjes

*Group members:* Zs. Baji, I. Bársony, Cs. Dücső, Z. Hajnal, A. L. Tóth, E. Holczer, and E. Tóth

Projects are supported by:

- OTKA K108366 - Creating microchannels by Proton Beam Writing and their applications in Lab-on-a-chip devices (2013-2017)
- ENIAC - Intelligent Catheters in Advanced Systems for Interventions – INCITE

Significant efforts were made in the MEMS Laboratory of MFA to set up a competitive infrastructure and focus a solid knowledge background for supporting the development of biosensors, biointerfaces and microfluidic systems. The developing scientific field concentrated around the micro- and nanofluidical, bioanalytical and medical diagnostic (BIOMEMS) research topics are highly challenging which is proven by the numerous research projects, the emerging industrial interest and the increasing number of interested students. The group – covering postdoc researchers, Ph.D. and graduate students – beyond the own scientific topics is able to efficiently support also the scientific research of national and international institutes, the developments defined by the industrial partners or education at the partner universities.

As a result of novel and innovative biosensing and sample preparation principles new possibilities in medical applications are being proposed. These bioanalytical systems are expected to integrate the micro and nanoscale transducers with sample preparation microfluidic systems also composing Lab-on-a-Chip devices. Our main goal is to develop *integrated devices and systems for industrial and medical applications*.

Besides the development of conventional micromechanical sensors, solid background was established at MFA for the research and development on bioanalytical and medical diagnostic systems, supported by a complex laboratory dedicated to the characterization and validation of microfluidic and BIOMEMS devices.

The established system technology is accessible for the Hungarian project partners (universities, industrial and institutional partners) and can be applied for realization of complex micro- and nanofluidical systems in silicon/glass and polymer materials.

Collaborations were established by the research project-participations in Hungary and abroad: ATOMKI, BME, ELTE (Biological Physics, Immunology Research Group), PPKE, SE, SZE, SZTAKI / Momentum Group of Róbert E. Gyurcsányi -

BME, Momentum Group of Róbert Horváth – MFA, Momentum Group of András Guttmann – Pannon University and the Companies: 77 Elektronika (Budapest, Hungary), AlphaSIP (Madrid, Spain), Ateknea Solutions (Budapest, Hungary), Biotalentum (Gödöllő, Hungary), Diagnosticum (Budapest, Hungary), FRK (Zabrze, Poland), Micronit (Twente, The Netherlands), NORMA Diagnostics, (Wien, Austria), Philips Research (Eindhoven, The Netherlands), Tateyama Kagaku Ind Corp. Ltd. (Toyama, Japan).

The technological and scientific results were directly transferred into the curricula of higher education institutions, which are represented by a number of students working in the laboratory towards their TDK (8 prize winners on university and national level), B.Sc., M.Sc. (16) or Ph.D. theses (1+3).

## **Microfluidic system for separation circulating tumour cells (CTC)**

Cell sorting has particular importance in cancer research since it can be applicable to remove the background cells from a limited volume of biological samples taken from blood or liquid biopsy. Dealing with a very small number of available cells in the samples makes Microfluidic Cell Capture Devices (MCCDs) promising tools for detection, capture and enrichment since the geometrical dimensions of the target cells and the working channels are in a similar order of magnitude. Due to their small dimensions (with the benefit of high surface to volume ratio), they can offer unusual physical behaviour that is different from that known in the macroscopic world.

The aim of this work was to design and fabricate a microfluidic device of special 3D geometry using conventional lithography based rapid prototyping and advanced Proton Beam Lithography (PBW) to improve the cell capturing efficiency. In order to increase the active surface area and the effective cross-section of the receptor microstructures they were doubly tilted. Preliminary Computational Fluid Dynamics (CFD) simulations revealed that tilting the pillars not only increases their surface area, across which the fluid can interact with the bonded affinity layer, but also improves the fluid characteristics of the system.

Special 3D structures were designed and fabricated by multiple tilted proton-beam writing method in SU-8 epoxy based negative photoresist and poly-dimethylsiloxane (PDMS) to enhance the cell capturing capability of the proposed microfluidic system. The developed 3D microstructure of the fabricated cell separation system was imaged by scanning electron microscopy as demonstrated in Fig. 1.

The PBW method proved to be successful for the irradiation of the microstructures under multiple angles. The advantage of direct writing method was also exploited for fast prototyping of microfluidic structures with various patterns. The demonstrated

PBW method assisted the fabrication of additive microstructures for microfluidic devices with special features otherwise unachievable by conventional microlithography techniques. Further advantage of the presented methodology is that the applied structural materials were compatible with MEMS/NEMS (micro/nano-electromechanical systems) technology considering the integration requirements for subsystem development.

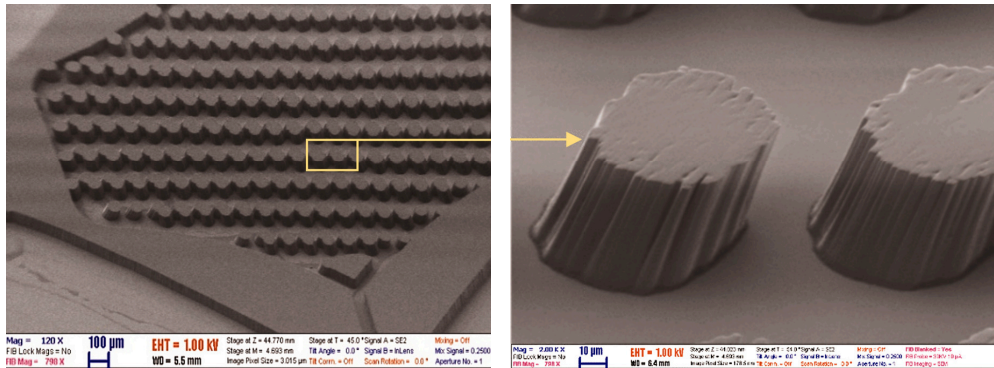


**Figure 1** SEM images of tilted micropillars in SU-8. The cylindrical pillars are raster-scanned to obtain the rippled edges required for improved capture efficiency (i.e., enhanced surface area).

## Finite Element Modelling (FEM) and characterisation of cell and molecular advection in continuous microfluidic systems

One of the key features of the bioanalytical devices is the sample preparation, which includes the dilution and complete mixing of the analyte with reagents of adequate buffer solution. The mixing is limited on microscale, since turbulent flow cannot occur due to the dominant viscosity. Chaotic advection can be considered as an ideal mixing method in microfluidic channels, so the modelling of this physical phenomenon is crucial for optimization the proposed systems.

Laminar Flow module of COMSOL Multiphysics was used to solve the velocity field of herringbone type micromixer to characterize fluid flow properties. For modelling the mixing phenomena two approaches were used. Mixing by diffusion along the channel was modelled with Transport of Diluted Species interface. To avoid numerical diffusion and high computational cost we used the Particle Tracing module to observe mixing at the particle-level. Secondary flow and the rotation caused by the herring-bone structure were clearly observable in the velocity field and Poincaré-map of particle trajectories in Fig. 1 and showed the layered structure of particle distribution.

To validate the computational results the modelled herring-bone mixer structures were implemented in polydimethylsiloxane (PDMS) microfluidic structures using rapid prototyping. Dye was used for the measurement of mixing by diffusion and yeast cells were used for the particle approach. The measurements confirmed the rotation caused by the ridges and also the layered flow characteristics.

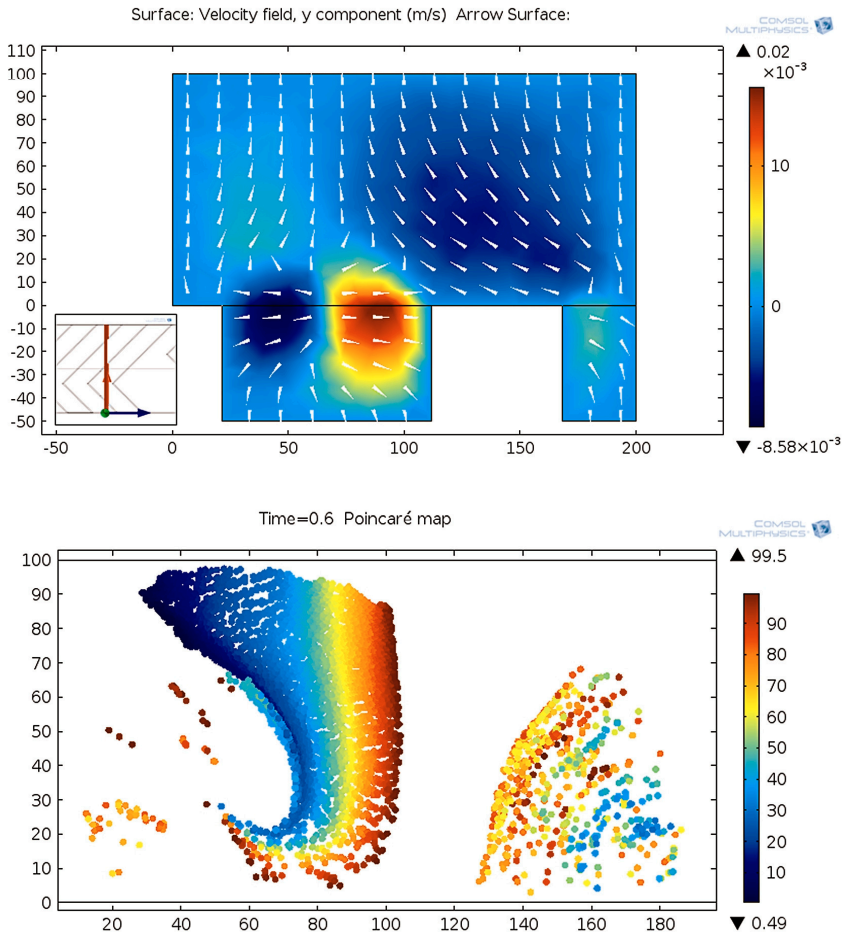


**Figure 1** Rotation caused by the ridges in the velocity field plane (top) and the Poincaré map of particle trajectories at the outlet (bottom). Color of particles denotes their initial y coordinates. Layered distribution is well observable.

## Autonomous microfluidic sample transport systems

Autonomous capillary systems could be substantial constituents of cheap, simple and self-powered microfluidic systems being capable to manage sample transport in Lab-on-a-Chip applications. Accordingly the precise control or improvement of the fluid conducting characteristics of these integrable micro pumps is in forefront considering their capacity and efficiency. Moreover the management of the achievable flow rate and the transported sample amount could be critical regarding various applications considering the requirements of controlled microreactors or high sensitive diagnostic devices also, and had to be adjusted by the geometric and surface parameters of the developed passive pump.

The microfluidic systems were fabricated by soft lithography in PDMS applying multi-layered SU-8 molding replica and bonded to glass substrates. The geometry and the 3D design of the channels were inspired by the most complex natural microfluidic system, the water-transport tissue (xylem) of trees and different geometric shapes were developed at the bottom of the channels like stripe and serpent type grooves. Due to its originally hydrophobic surface characteristics, the applied PDMS was modified to improve its wettability by embedding different concentrations of amphiphilic molecules (TX-100 and PDMS-PEO) in the matrix before polymerization. The combined effects of different 3D geometries and surface modifications were systematically characterized by flow rate measurements, by applying an ultra-fast imaging system for recording fluid movement. The surface modification methods were compared, and the advantages of bioinspired capillary systems were also demonstrated.

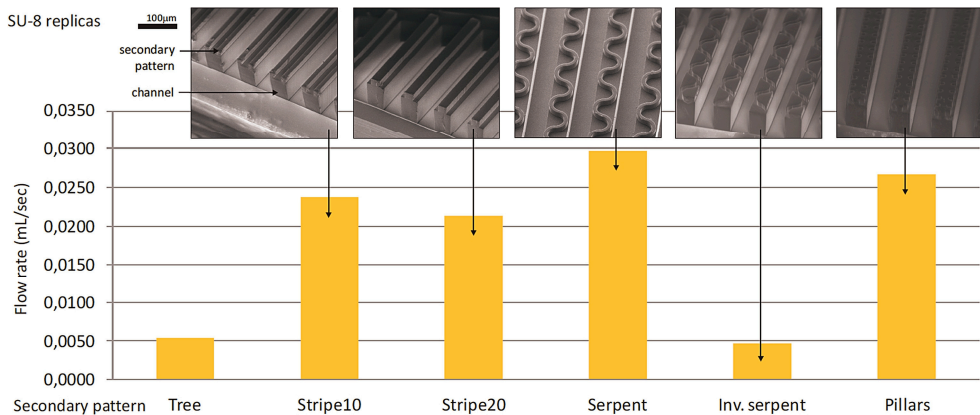


**Figure 1** The combined effects of different 3D geometries and surface modifications were systematically characterized by flow rate measurements applying ultra fast imaging system for recording fluid movement.

We can conclude that the efficiency of the microchannel based capillary pump systems can be improved by applying adequate micro-patterning (as groves) and additional surface modification, facilitating the development of enhanced passive capillary pump systems.

## Micromachined coplanar dielectric barrier discharge plasma system

A micromachined coplanar dielectric barrier discharge (DBD) plasma system was constructed as integrable plasma sources for Lab-on-a-Chip and other analytical applications. Their relevant advantages are the simplicity, flexible and down-scalable geometric structure, low power consumption, precisely tailored functional parameters and integrability into micro-analytical systems. The microplasma-source was manufactured by the combination of conventional micromachining technology and microchannel structuring methods to form coplanar electrode system in compact microfluidic and reactor chamber.

### Switchable microfluidic capillary pump system

The precise and effective sample transport is a substantial task of the microfluidic systems in chemical and biomedical applications, ensuring controlled flow through the sample preparation system. Passive pumping systems are promising candidates considering the price and complexity of the microfluidic cartridges. From economic aspects the application of polymers as structural materials in the fluidic systems is also advantageous, however, the mainly hydrophobic behaviour of these materials is a critical point. In our approach an electrically controlled, local and in situ surface modification method was developed and validated in polymer based microstructures.

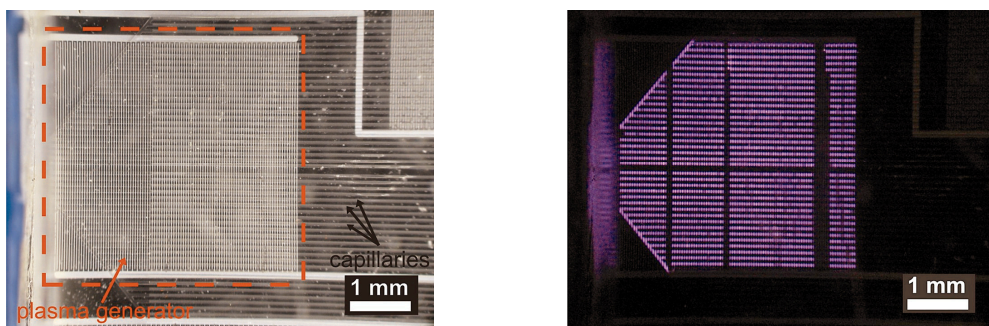


**Figure 1** The DBD plasma source covered with PDMS based capillary system (left) and the plasma generated locally in the channels (right).

A microfabricated coplanar dielectric barrier discharge (DBD) plasma source was developed, integrated and applied to modify *in situ* the surface properties of polydimethylsiloxane (PDMS) capillary channels. The local, immediate, and successful setting of the wettability of the polymer microchannels is proven by the development of effective water transport in the system following the plasma treatment. *In situ* modification of originally hydrophobic polymer surfaces by local plasma-enhanced oxidation and its application in electrically controlled fluid capillary systems are demonstrated. The use of microfluidically integrated DBD microplasma system such as in a switchable capillary pump is also presented.

The atmospheric pressure Dielectric-Barrier Discharge generated microplasma can find applications in: CO<sub>2</sub> lasers, UV lamps, plasma displays and in ozone generation, water pollution control or local surface treatment. The applicability of these plasma sources in molecular emission spectroscopy for environmental analysis is also looked at.

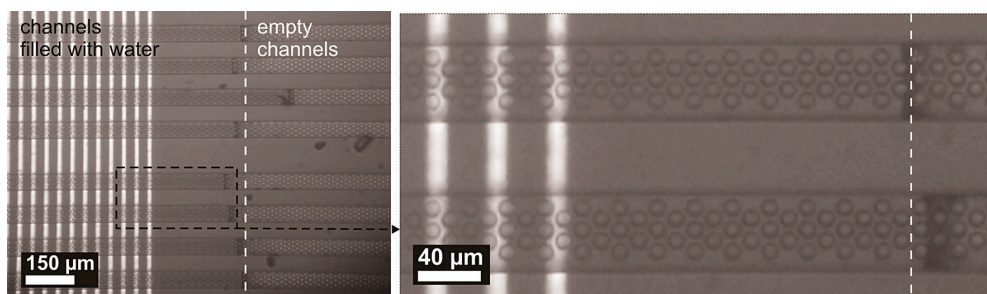


**Figure 2** Capillary channels crossing the plasma source, filled with water.

The developed microplasma chamber was tested as gas plasma source by recording emission spectra of various injected gases and organic solvent vapours mixed in N<sub>2</sub> precursor. The functional parameters of the miniaturized DBD micro plasma generator were determined while the device was operated at atmospheric pressure. The molecular composition in the micro plasma chamber was monitored by optical spectrometer, and the feasibility of the source for spectroscopy was demonstrated by the detection molecular emission spectra of test gases and vapours. CO<sub>2</sub> and organic solvent vapour were injected and the change in detected molecular emission spectra were analysed qualitatively. These results promise the possible integration DBD microplasma excitation source in emission spectroscopy based micro- analytical systems containing (microfluidic) sample preparation functions, too.

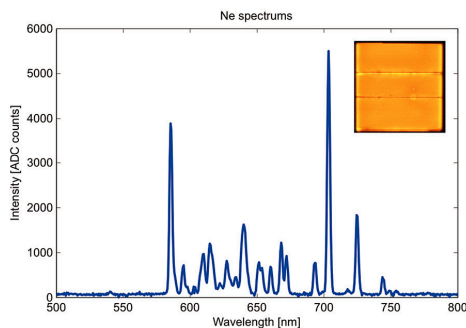
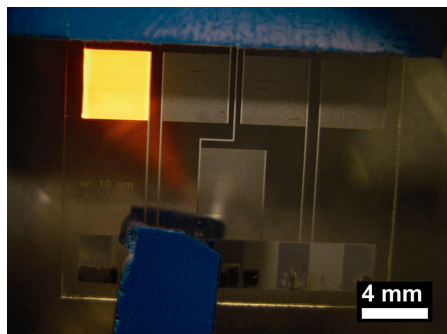


**Figure 3** Working DBD microplasma generator in Ne atmosphere (left) and the emission spectra recorded.

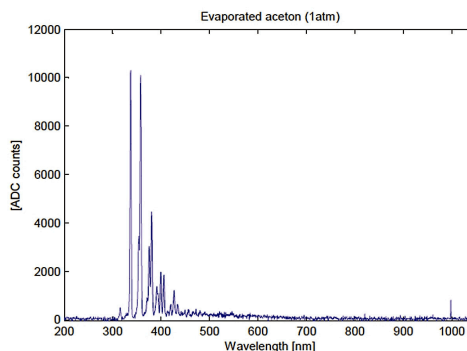
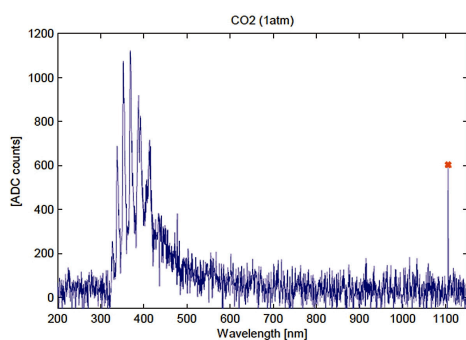


**Figure 4** Recorded optical emission spectra of  $\text{CO}_2$  gas and Acetone vapour mixed in  $\text{N}_2$  precursor injected and excited in the microplasma chamber.

## Solid state nanopore and nanocapillary based integrated bioanalytical systems

Solid-state nanopore arrays provide promising *novel solution for label-free and multi-parametric detection of macro- and submolecules* at extremely low concentration in various biosensor applications. Recently, these nanopore structures received a lot of attention primarily due to the prospect of using them as third generation DNA sequencers but also as new (bio)chemical sensing platforms. Solid-state nanopore arrays could provide effective solution for development integrated Lab-on-a-Chip systems for sensitive molecule recognition; however, their electrical parameters are strongly correlated to the effective size and conformation of the pores.

Nanopore-array membranes were fabricated by the combination of silicon micromachining and subsequent nanofabrication techniques. In order to prove the suitability of the nanopore arrays for electrochemical measurement, the fabricated membranes were addressed fluidically and electrically parallel by additional microfluidic cartridge and holder. The integrated nanopore platform in biosensor application is based on two different in-pore molecule binding processes. Each integrated nanopore array contained 64 pores with the nominal diameter  $50 \text{ nm} \pm 10\%$ . The sensing principle based on the transport modulation through the nanopore was validated by the detection of successful biotin-avidin and aptamer - hIgE binding processes using electrochemical impedance spectroscopy (EIS).

For preliminary validation standard avidin-biotin binding complex was implemented. The inner pore surfaces were previously functionalized by biotin molecules applying thiol chemistry and the binding of the targeted avidin molecules was followed through the changes of the nanopore-membrane impedance measured in time by EIS and demonstrated in Fig. 1.

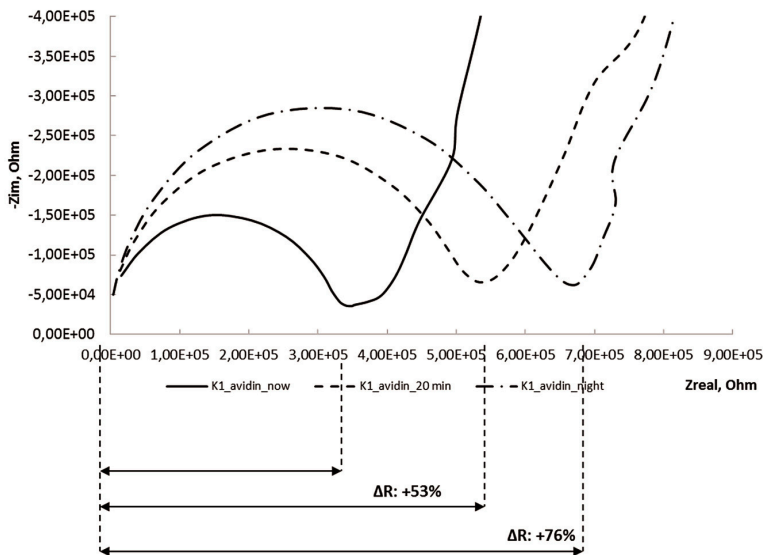


**Figure 1** EIS results and resistance change of the integrated solid-state nanopore array after injection  $0.1 \mu\text{M}$  avidin/PBS solution, after 20 mins and after one night respectively.

The second step was focused on the recognition of the in-pore hIgE specific aptamer – human-immunoglobulin-E (hIgE) binding process. In case of the hIgE binding experiment the membrane resistance ratio ( $R/R_0$ ) of the functionalized chip was also increased significantly after introducing  $10 \mu\text{g/ml}$  hIgE, while the reference chip's signal changed slightly. Both experiments proved the suitability of the integrated system for the proposed point-of-care biomedical device utilizing the presented label-free bioanalytical detection methodology.

## **NeuroMEMS**

*Activity leader:* Z. Fekete

*Group members:* P. Fűrjes, Z. Hajnal, Gy. Molnár, A. Pongrácz, A. L. Tóth, Z. Bérczes, and G. Márton

Projects are supported by:

- Targeted research activity supported by Gedeon Richter Plc.

### **Neural Cell Response to Nanostructured Biosensor Surfaces**

Cells in their natural environment interact with nanoscale structures like the extracellular matrix and its proteins. Based on biomimetic consideration, creating nanopatterned implant surfaces promises better cell adhesion, and therefore better biocompatibility. By modulating the specific surface area, wetting and nano-pattern regularity of the nanostructured samples, several groups published better neural cell adhesion and viability on nanostructured surfaces compared to the smooth references in the past few years.

Our work aims to synthesize bioimplant surfaces with nanoscale patterns using novel combination of micro- and nanomachining techniques. The proposed maskless nanopatterning method can easily be integrated into the fabrication process of neural microelectrodes. The expected results are envisioned to minimize the immune response of the neural tissue to the surface of the implanted microelectrodes and thus enable efficient functionality in long-term experiments.

Nanostructured samples were reproducibly fabricated with various surface morphologies using deep reactive ion etching.

Different surfaces were characterized morphologically and electrochemically. We also examined samples with surface adhesive proteins, usually used for neural cell culturing. This way, misinterpretation of in vitro results due to possible planarization effects is minimized. Cell adhesion protein coating was carried out at the Research Institute for Experimental Medicine, HAS. The proteins were PLL (Poly -L-lysine) and AK-c(RGDfC). PLL is an artificial protein for neural cell culturing. AK-c is a synthetic adhesive polypeptide especially for neural progenitors.

The specific surface area of the nanostructured and platinised samples were recovered from cyclic voltammetry measurements. Electrochemical impedance spectroscopy was carried out to show the impedance reduction, which also refers to surface area enhancement.

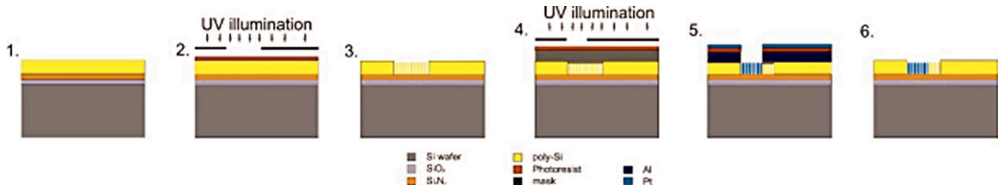


Figure 1 Schematic process flow of the sample fabrication.

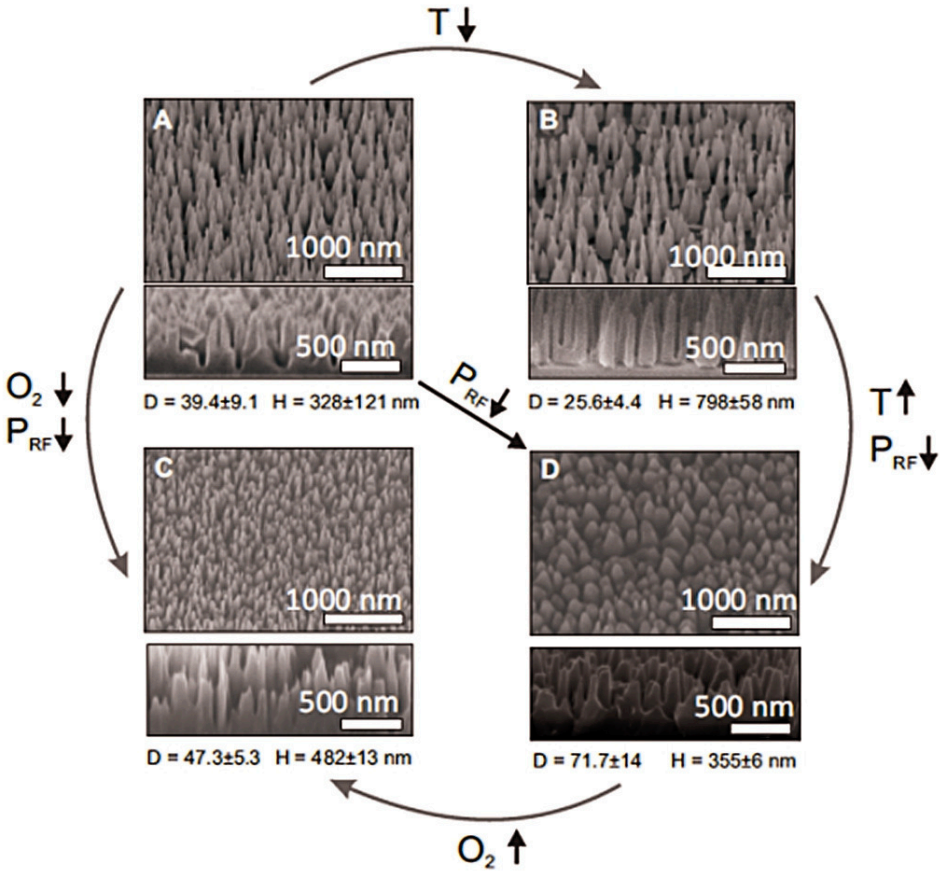
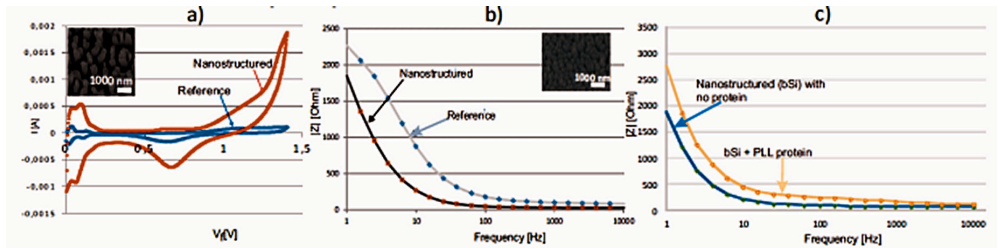


Figure 2 DRIE parameter dependence of nanopillar density and height.

Since wetting of several surface morphologies apparently influences cell adhesion, it was characterized by contact angle measurements. A representative change in contact angle can be seen on Fig. 4.

GFP-NE-4C cell lines (mouse brain neuroectodermal cells) were cultured on the micropatterned, and nanostructured surfaces, and were analyzed by fluorescent microscopy. Remarkably, compared to the nanostructured ones more cells adhere on

flat surfaces. Neural and glia cells will be investigated on the surfaces in the near future for more accurate estimation of in-vivo biocompatibility.



**Figure 3** 30 times larger specific surface area was measured by a) CV and b) EIS. c) Significant impedance increase on the protein coated samples.

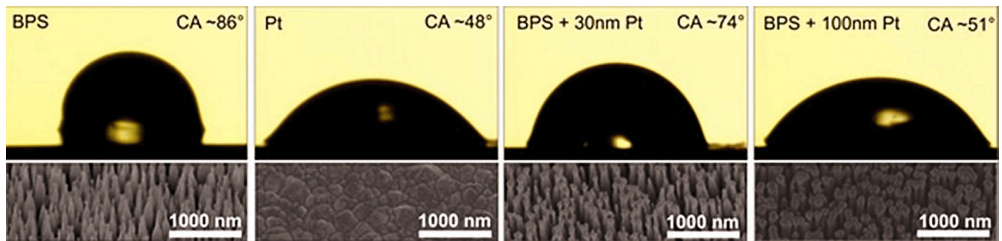


**Figure 4** Effect of surface nanostructuring and metallization of BPS surfaces on static contact angle.

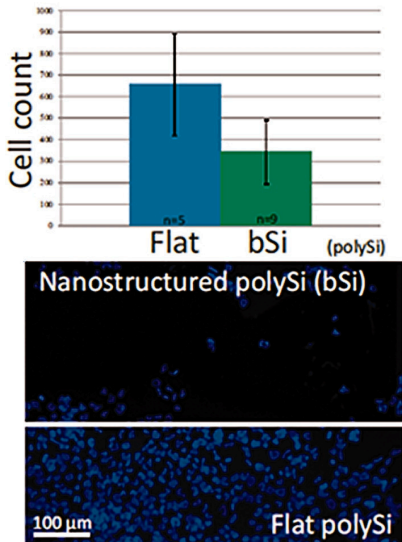


**Figure 5** Cell counts on flat poly-Si and nanostructured poly-Si surfaces.

## Optrode for multimodal deep-brain infrared stimulation

In recent years, optical stimulation in neuroscience has emerged as an alternative to electrical stimulation. Infrared neural stimulation (INS) has a number of advantages compared to electric stimulation. INS does not produce recording artefacts (cross-talk) in the electrical signal, allowing recording close to the stimulation in both space and time. The stimulated volume is controlled by the outcoupled intensity profile, which is a design parameter of a stimulation system. Compared to optogenetics, this method lacks of the sensitizing step, which is both an advantage and disadvantage in terms of experimental difficulty with respect to the greater control of optogenetic stimulation. The interest in this stimulation method is increasing, demonstrated by the various applications of INS.

Infrared neural stimulation (INS) was discovered by Jonathon Wells and his team in 2005. The stimulation employed a pulsed infrared beam of varied wavelength and intensity to evoke action potentials. Later studies revealed that there is a wavelength-dependent radiant exposure range where action potentials are evoked without cell damage.

The aim of our work is to present a tuneable optrode capable of integrated optical stimulation and electric recording. The system combines the advantages of silicon microfabrication and silicon's transparency in the near-infrared. For efficient coupling into the probe and controlling the illuminated volume in the brain, silicon microlenses were simulated using MATLAB. The lens system can focus light in 2D, with configurable focal length and spot size.

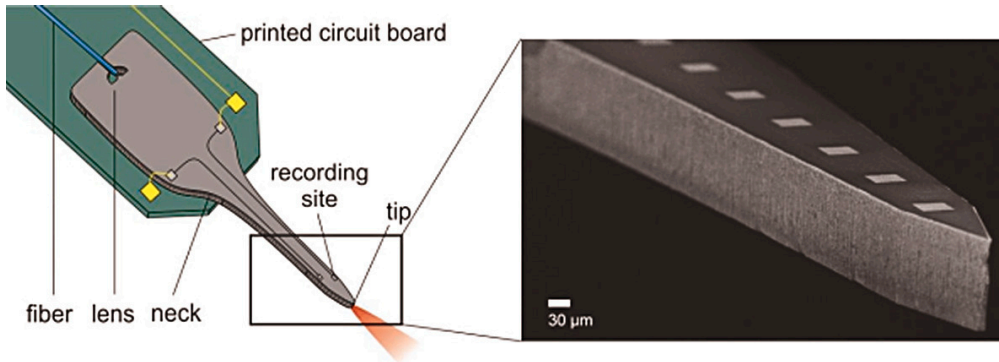


**Figure 1** Concept of the stimulation/recording system. Inset: SEM micrograph of the tip of the Si microelectrode.

The manufactured lens system has two purposes: efficient coupling from an optical fibre to the shaft of the probe and coupling out from the shaft. When coupling in, the lens-fibre distance is determined, so that the rays are approximately parallel and the spot on the tip is the smallest. Since there is some aberration due to the fibre being a line source in 2D, a single mode fibre is used. The fibre – lens distance is kept small enough to exploit the whole cone hitting the probe. For coupling out, a parabolic

mirror is used to direct the light in the vicinity of the shaft, stimulating sufficiently close to the recording sites.

When evaluating the results of the simulation, the main problem is the sensitivity to the placement of the fibre. While the parabolic mirror focuses the rays to the same point, the coupled out beam's angle changes to a large extent even in case of small difference in fibre position (Fig. 2a). Since the critical angle is large, this implies that coupling out through a flat surface has a very limited acceptance angle.

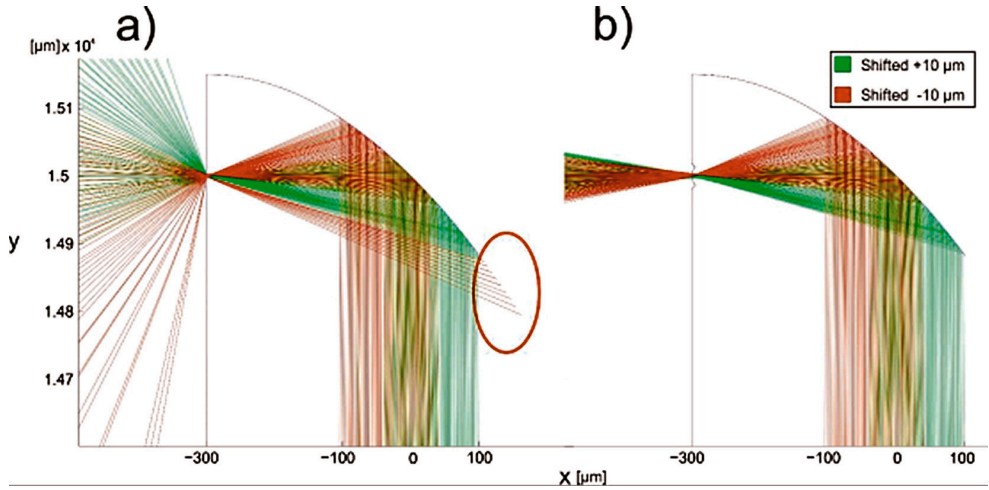


**Figure 2** Decreasing the sensitivity of the optical system: a) no supplementary lens; b) negative supplementary lens. Highlighted: rays reflected because of the small acceptance angle.

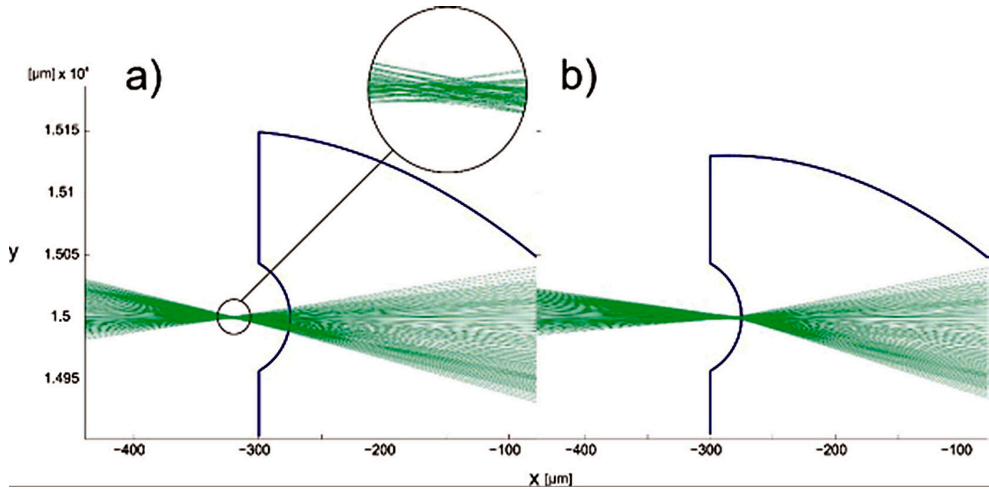


**Figure 3** Supplementary lens used to control focus distance from probe. a) 45  $\mu\text{m}$  from probe b) 5  $\mu\text{m}$  from probe. Inset: rays near focused area, showing aberration.

To overcome these limitations, an additional lens is placed opposite to the parabolic mirror. This lens can be configured to act as a supplementary optical element. A lens surface of negative radius can be used to greatly decrease sensitivity of the out-coupled rays to the position of the optical fibre. The lens transforms a large angle difference to a small position difference (Fig. 2b). By moving the lens further away from the parabolic focus point, the beam can be enlarged to illuminate a larger volume. A surface of positive radius can be used to create a configuration, where light is focused inside the tissue. Since the parabolic mirror introduces coma, the light is focused into a small cross-section rather than to a point. This solution offers the opportunity to tune the optical power to maintain stimulation threshold in the focused area. Changing radii of lenses can be used to set the position of area in focus (Fig. 3).

## A polymer-based spiky microelectrode array (MEA) for electrocorticography

Polymer-based MEMS devices are gaining increasing attention in the field of electrophysiology, since they can be used to form flexible, yet reliable electrical interfaces with the central and the peripheral nervous system.

We have manufactured MEAs with PI bottom insulator,  $\text{TiO}_x + \text{Pt}$  conductive and SU-8 top insulator layers, and found that this structure of microfabricated layers allows a rapid and reliable technological process flow. Acute *in vivo* functional tests on rat cortex were performed. The 24 electrodes cover a 1.15 mm long linear section of the tissue, thus they make possible obtaining detailed electrophysiological record-

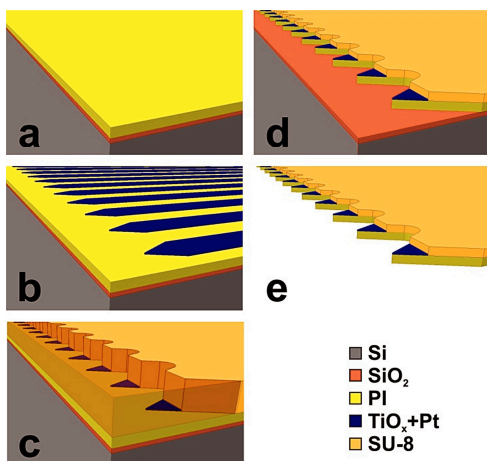


**Figure 1** Schematics of the fabrication process steps. Two photolithographic masks are utilized, the first in step (b) for patterning the metal layer and the second in step (c), for patterning the top SU-8 layer.

ings of a small area, containing neighbouring cortical columns. The polymer-based device is not as stiff and fragile as silicon-based neural probes, however, due to its relatively wide shaft; it is not suitable for implantation into deep areas. The arrow-like electrodes protruding from the shank allow a slight penetration into the tissue, which is not typical of commonly used polymer-based ECoGs. On the other hand, this feature makes our device more invasive compared to them. The 27  $\mu\text{m}$  thick PI-SU-8 layer-compositions at the bulk of the device and the single 7  $\mu\text{m}$  thick PI layer beneath the electrodes have proven to be able to provide sufficient mechanical robustness for the electrode array to endure interfacing with the neural tissue.

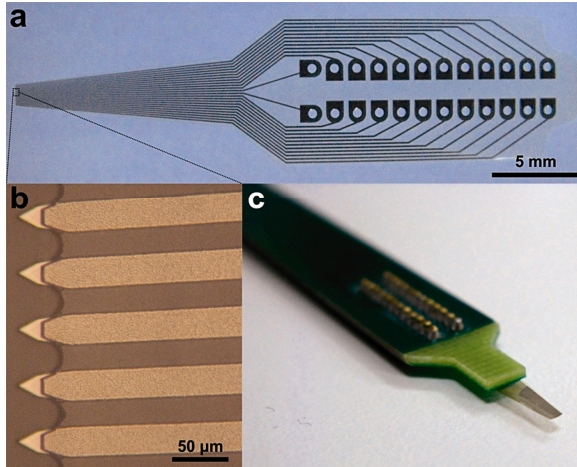


**Figure 2** (a) The microfabricated component contains with electrodes, corresponding bonding pads and lead wires. The bottom PI and top SU-8 isolating polymer layers are almost totally transparent. (b) Image of the spiky electrode array at the tip. The center-to-center distance of the sensors is 50  $\mu\text{m}$ . (c) The microfabricated component mounted on a PCB. The MEMS component is turned over, so the electrode surfaces are facing downwards.

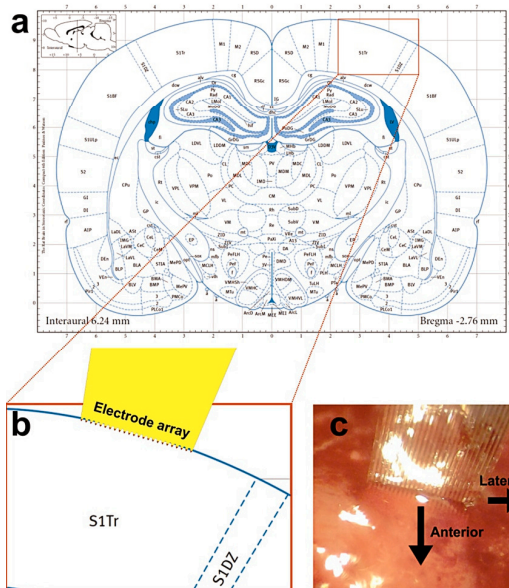


**Figure 3** (a) Coronal section of the rat brain -2.76 mm posterior to the bregma. Illustration is based on Figure 56 of (Paxinos & Watson 2009). (b) Zoomed view of a somatosensory area and a proportional representation of the MEA on the cortex. (c) Microscopic image the *in vivo* use of the device.

## **NEMS**

*Activity leader:* J. Volk

*Group members:* Zs. Baji, G. Battistig, Cs. Dűcső, P. Földesy, N. Q. Khánh, I. Lukács, Gy. Molnár, A. L. Tóth, Zs. Zolnai, R. Erdélyi, Z. Szabó, and I. Bársony

Projects are supported by:

- OTKA K109674 – Graphene-based terahertz modulators (2013-2017)
- FP7-ICT-2013-10- 611019 - High-resolution fingerprint sensing with vertical piezoelectric nanowire matrices (PiezoMAT) (2013-1015)

### **Effect of Seed Layer Post-deposition Annealing on the Vertical Alignment of Epitaxially Grown ZnO Nanowires**

Vertically aligned ZnO nanowires (NWs) are attracting a great interest due to a variety of splendid applications. The most actively researched fields are electronics, optoelectronic-, and electromechanical nanodevices. In the last one and a half decades a number of such devices were demonstrated, e.g., solar cells, field emission devices, UV lasers, light emitting diodes, and nanogenerators. As well as their diverse needs in terms of functionalisation and device structure, each of these applications has different requirements in terms of the degree of nanostructure alignment. Synthesis of vertically aligned NWs can be achieved by both physical methods at high temperature and chemical methods at low temperature. However, the precise tuning of the NWs' vertical alignment in a relatively wide range on the same substrate material was not reported yet. Here we demonstrate that post-deposition annealing of the ZnO seed layer before NW growth is a powerful tool for tuning the vertical alignment of homoepitaxially grown ZnO NWs.

The vertical ZnO NW bundles were synthesized by our selective area wet epitaxial growth method on a 200 nm thick CVD ZnO/Si(111) layer. Before NW growth 4 of the samples were annealed in N<sub>2</sub> atmosphere at different temperatures for 2 hours in a quartz tube furnace: at 300 °C, 500 °C, 700 °C, and 900 °C. The 5<sup>th</sup> reference sample was left without post-deposition annealing. AFM study of the surfaces revealed that the grain sizes of the CVD ZnO seed layers in the lateral direction increased with increasing post-deposition annealing temperature as the result of coalescence (Fig. 1).

As we have shown earlier by quantitative XRD and AFM analysis, the crystal quality and alignment of the NWs is determined by the dispersion in the crystallographic orientation of the seed layer while the effect of the surface roughness

is negligible. Fig. 2a shows the XRD  $\theta/2\theta$  scan curves of the reference sample and the seed layers annealed in  $N_2$  in the  $2\theta$  angle range from  $30^\circ$  to  $38^\circ$ . Only diffraction peaks of ZnO(0002) index planes appear in these curves proving that the films are

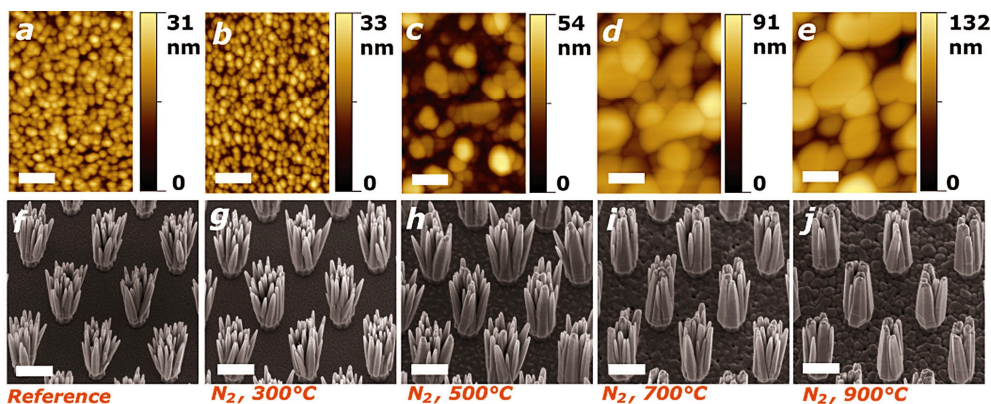


**Figure 1** AFM height images of the CVD ZnO seed layers annealed at different temperatures (a-e). Perspective view SEM micrographs of the corresponding ZnO nanowire bundles grown on the different ZnO seed layers (f-j). The length of the white scale bars on the AFM and SEM images is 200 nm and 1  $\mu\text{m}$ , respectively.

strongly c-axis oriented. The inset shows the (0002) reflection in a narrower range. It is clearly seen that higher annealing temperature results in a narrower and higher (0002) peak. The dispersion in the crystallographic alignment of the seed layers can be estimated from the  $2\theta/\chi$  mapping around the (0002) peak using the 2D-detector system: FWHM along the  $\chi$  direction – which is inherited by the corresponding epitaxial NWs – has to be compared for the different layers. Fig. 2b-f show the 2D XRD patterns for the different seed layers. It can be seen, that  $\chi$  FWHM is the lowest after 900 °C annealing and the highest without annealing or after 300 °C. Hence it indicates that the former is the most highly oriented while the latter two are the most disordered, consistently with the corresponding SEM images of Fig. 1.

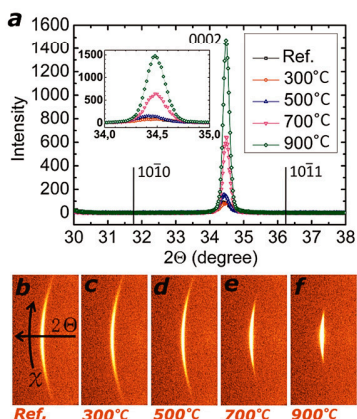


**Figure 2** Characteristic  $\theta/2\theta$  scan curves of the reference sample and the seed layers annealed in nitrogen in the  $2\theta$  angle range from  $30^\circ$  to  $38^\circ$  (a). The inset shows the magnified (0002) peak for each layer. 2D XRD patterns showing the (0002) reflection for the same layers recorded by the 2D detector: no postdeposition annealing (b), annealed in  $N_2$  at 300 °C, 500 °C, 700 °C and 900 °C (c,d,e, and f, respectively).

## Mechanically Gated ZnO Thin Film Transistor for Nanoelectromechanical Sensing

Several mechanical sensors operating on different principles were already demonstrated in the sub-millimeter range, such as the piezoresistive tactile sensor developed at MFA and distributed by TactoLogic Ltd. However, integrated device being suitable for direction dependent force detection in the sub-micrometer range has not been demonstrated yet. Due to its small dimensions and its piezoelectric behaviour – which causes, for instance, the appearance of an electric potential difference between its tensed and compressed sides in response to bending – a ZnO nanowire (NW) can operate as building block of such a device. According to finite element simulations the piezoelectric potential difference (and the mechanical stress as well) occurring as the result of bending takes place not only between the two sides of the NW, but inside the whole depth of the ZnO seed layer under the NW as well. Hence the resistivity of the seed layer can be modulated by mechanical strain which can be the basis of a nanomechanical sensor. The origin of the device's operation could be either the coupled piezoelectric and semiconducting nature of the seed layer or its piezoresistivity as well. In order to exploit this phenomenon and demonstrate the NWs' applicability for nanomechanical sensing we developed a ZnO thin film transistor, in which the source-to-drain current is modulated by mechanical strain instead of a voltage applied to the gate electrode.

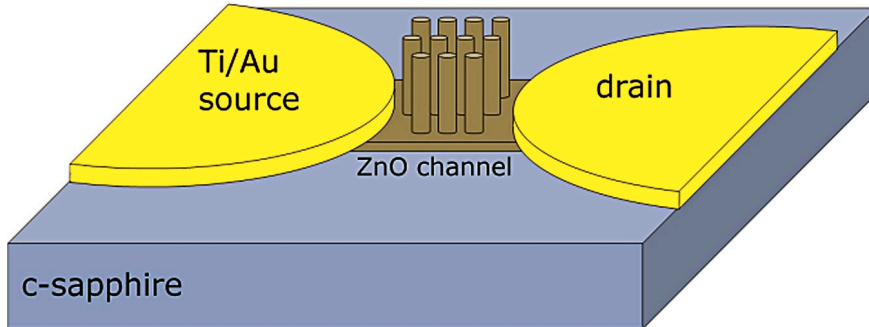


**Figure 1** Characteristic  $\theta/2\theta$  scan curves of the reference sample and the seed layers annealed in nitrogen in the  $2\theta$  angle range from  $30^\circ$  to  $38^\circ$  (a). The inset shows the magnified (0002) peak for each layer. 2D XRD patterns showing the (0002) reflection for the same layers recorded by the 2D detector: no postdeposition annealing (b), annealed in  $N_2$  at  $300^\circ\text{C}$ ,  $500^\circ\text{C}$ ,  $700^\circ\text{C}$  and  $900^\circ\text{C}$  (c, d, e, and f, respectively).

The schematic of the device is shown in Fig. 1. A thin ZnO stripe (width:  $3.1\ \mu\text{m}$ ) was wet chemically etched from a heteroepitaxial ZnO layer (thickness:  $25\ \text{nm}$ , sheet resistance:  $52\ \text{k}\Omega/\square$ ) above an insulating c-sapphire. Afterwards, two metal electrodes (Ti  $30\ \text{nm}$ /Au  $70\ \text{nm}$ ) were deposited covering the two ends of the channel. The channel length between the metallization was  $3.6\ \mu\text{m}$ . The structures were defined by a laser pattern generator using photoresist. In order to make good Ohmic contacts and minimize the resistance of the ZnO-metal junctions the sample was

annealed in a rapid thermal annealing process in  $N_2$  atmosphere. An array of vertical ZnO NWs was grown on the top of the ZnO channel. The metal electrodes were contacted by wire bonding.

Fig. 2b shows the FE-SEM image of the device. The electromechanical behaviour in response to NW bending was studied by AFM bending experiments. The sample was mounted inside the AFM and a constant bias of 0.2 V was applied between the source and drain electrodes. The voltage was applied by the source-meter unit (c-unit) of the microscope by which the resulting current was also monitored. In order to visualize the lateral and normal forces acting between the probe and the NWs the lateral and normal output of the AFM position sensitive photo detector (PSPD) were recorded. Hence the NWs were bent at their free end by the apex of the probe as shown schematically in Fig. 2a. Lateral and normal PSPD output signals in constant height mode, i.e. without feedback, were recorded simultaneously together with the current flowing through the channel. The probe was electrically insulated from the microscope. Hence, we obtained a resistivity modulation of 3 % of the conducting channel as a result of elastic bending of the NWs. The geometry optimization and further systematic quantitative electromechanical investigation are under process.

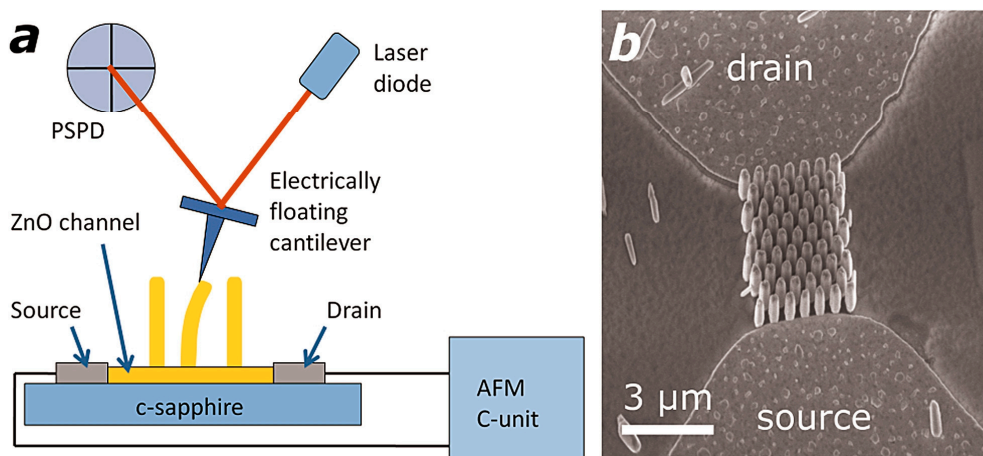


**Figure 2** Schematic representation of the measurement for the electromechanical characterization of the device. The NRs are bent by an AFM probe, while the current flowing through the ZnO channel is monitored (a). SEM image of the NW array on the ZnO conducting channel lying between two Ti/Au electrodes (b).

## Preparation of TiO<sub>2</sub> nanotubes with atomic layer deposition and hydrothermal growth

Titanium dioxide is one of the most widely examined compound semiconductors in materials science, due to its exceptional biocompatibility and versatility in applications such as photocatalysis and organic solar cells. TiO<sub>2</sub> nanotubes can be fabricated by the electrochemical iodization of TiO<sub>2</sub> sheets, sol-gel methods, and growth from templates. A drawback of most methods is that the as-grown structures have an amorphous crystalline structure and have to be annealed at high temperatures to transform them into crystalline phases. As the versatility of the prepared titania structures depends largely on the crystallinity (anatase phase is generally used in charge-separating applications and photocatalysis, rutile is widely used as dielectric layers and for sensing applications), this is an indispensable step. The advantage of atomic layer deposition (ALD) for the preparation of titania is that the properties of the grown material can be controlled with the deposition conditions.

Ordered TiO<sub>2</sub> nanotube arrays were prepared by a combination of ALD and hydrothermal growth. First, a ZnO layer was deposited by ALD providing a homoepitaxial template for the subsequent hydrothermal growth. PMMA layer was patterned by e-beam lithography to define nucleation windows for the ZnO nanorods which were grown by aqueous chemical method. They were afterwards conformally coated by TiO<sub>2</sub> using ALD. After infiltrated the core-shell nanorod structure by photoresist the end of the rods were opened by plasma etching, and the ZnO core was removed by chemical etching.

The advantages of the method besides the nanotube array being well ordered is the easy control of the crystallinity and composition, as well as the easy doping of the TiO<sub>2</sub> material by the ALD method.

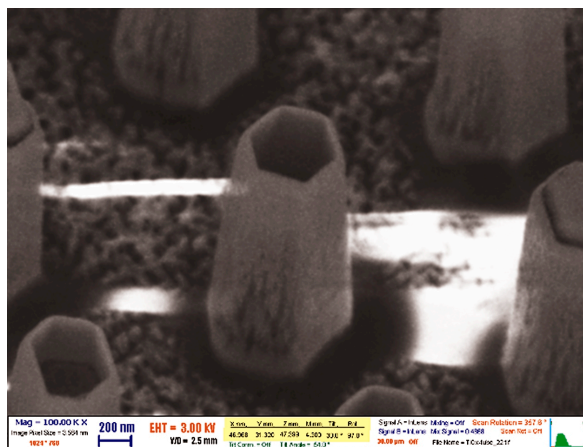


**Figure 1** TiO<sub>2</sub> nanotubes prepared by atomic layer deposition and hydrothermal growth.

## Metallization Aspects in Ultra Low Dimension TiO<sub>2</sub> Nanowire Based FET Fabrication

Though the quasi 1D nanostructure of the wide band gap semiconductor titanium dioxide (TiO<sub>2</sub>) is known as potential candidate for sensor, electronics and optoelectronics applications, the fabrication of a Field Effect Transistor (FET), a basic element based on the TiO<sub>2</sub> nanowires (NWs) with ultra-low dimensions (few nm wide and few tens nm long) still remains a challenge. To address this issue, we have developed a technique for contacting such small TiO<sub>2</sub> NWs, in which Atomic Force Microscope (AFM) has been used to find the adequate contacted NWs after very thin contacting metal layer formation. Then the second metal is to be deposited to make a connection between the leads and the contact pads (Fig. 1).

However, oxidation of the first metal surface during AFM measurement in ambient gives rise to non-ohmic conduction with very high resistivity at the metal/metal interface. To overcome this problem we have carried out an experiment (Fig. 2) to find the proper multi-layer of metals for contacting.

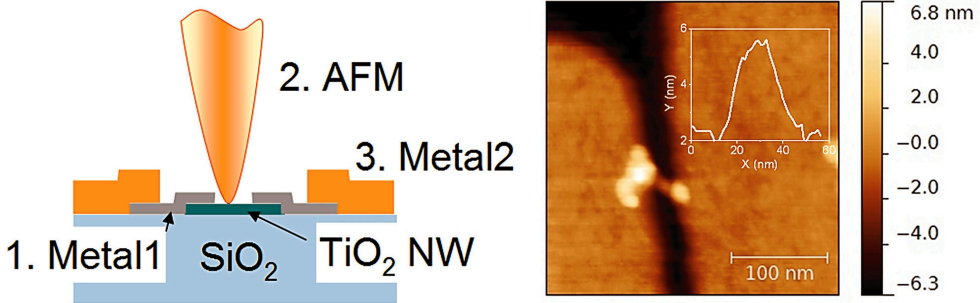


**Figure 1** Concept of TiO<sub>2</sub> NW contacting (left), and the contacted NW found by AFM after the first metallization (right). The line-cut across the nanowire is shown in the inset.

As shown in Table 1, oxidation of Ti makes the conduction non-ohmic even for the as-prepared layer. It becomes worse, i.e. the resistance increases by two orders of magnitude after heat treatment at 175 °C. The same behaviour has been observed for Cr, which excludes the use of solely Ti or Ti/Cr for metallization. In contrast, multi-layer with Au on top gives low and stable resistivity even after long time. The surface roughness change measured by AFM after annealing is about 10% for Ti and Ti/Cr. However, it is more than 50% in the case of Ti/Cr/Au annealed at 175 °C, which is the outcome of the contraction of thin Au layer at elevated temperature, so the Au layer consists of islands. Therefore, thin Cr layer was added to protect Ti underneath from oxidation. In spite of island-like structure of Au layer, the conduction is ensured well through the Au islands, so this multi-layer structure may be an adequate choice for the first metallization in our approach for fabrication of ultra-low dimension TiO<sub>2</sub> NW based FET.

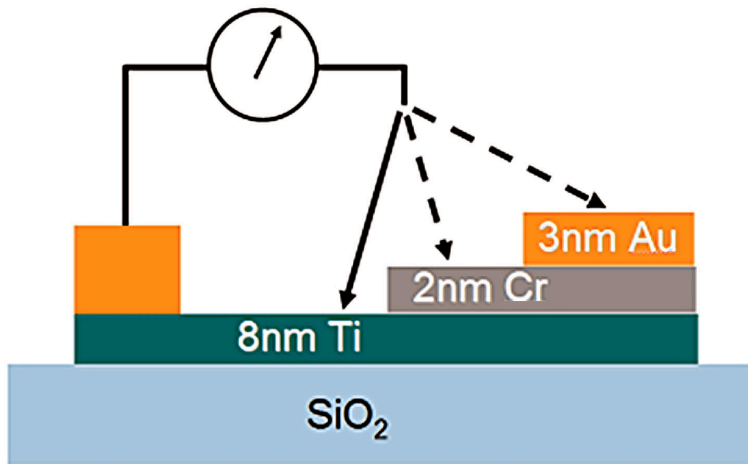


**Figure 2** Sketch of the multi-layer metal sample and I-V measurements.

5 min.	8nm Ti (k $\Omega$ )	+2nm Cr (k $\Omega$ )	+3nm Au (k $\Omega$ )
RT	1.250*/-	0.294/-	0.178/0.178
75 °C	0.833*/-	0.833*/-	0.480/0.500
175 °C	208.4*/-	111.1*/-	0.667/0.667

\* non-ohmic

**Table 1** Resistances of different metal layer structures (as-deposited/after 1 week in air).